Finite deformation effects in soft elastohydrodynamic lubrication problems[☆]

Stanisław Stupkiewicz[a,*], Jakub Lengiewicz[a], Przemysław Sadowski[a], Stanisław Kucharski[a]

[a] *Institute of Fundamental Technological Research (IPPT), Polish Academy of Sciences, Pawińskiego 5B, 02–106 Warsaw, Poland*

Abstract

Soft elastohydrodynamic lubrication regime is typical for many elastomeric and biological contacts. As one or both contacting bodies are then highly compliant, relatively low contact pressures may lead to large deformations which are neglected in the classical EHL theory. In the paper, the related finite-deformation effects are studied for two representative soft-EHL problems. To this end, a fully-coupled nonlinear formulation has been developed which combines finite-strain elasticity for the solid and the Reynolds equation for the fluid, both treated using the finite element method with full account of all elastohydrodynamic couplings. Results of friction measurements are also reported and compared to theoretical predictions for lubricated contact of a rubber ball sliding against a steel disc under high loads.

Keywords: lubrication, soft-EHL problem, finite deformation, finite element method, monolithic scheme

1. Introduction

An increased interest in soft elastohydrodynamic (elastic-isoviscous) lubrication regime is recently observed which is due to numerous applications in technology (elastomeric seals, tyres, etc.), but also because this lubrication regime occurs in many biotribological systems (e.g., synovial joints, human skin contact, oral processing of food, etc.), see, e.g., [1–3]. Several aspects

[☆]Published in *Tribol. Int.* 93:511–522, 2016, doi:10.1016/j.triboint.2015.03.016

*Corresponding author. Email address: sstupkie@ippt.pan.pl

of lubricated soft contacts have already been studied experimentally, such as the influence of load and elastic properties [4], non-Newtonian effects [5], and surface wetting [5, 6]. Experimental investigations of the roughness effects and of the transition from hydrodynamic to boundary lubrication can be found in [6–8], see also the related theoretical studies in [9, 10].

Contrary to the more popular hard-EHL contacts operating in the elastic-piezoviscous regime, the pressure is relatively low in the soft-EHL contacts. Nevertheless, the elastohydrodynamic coupling is crucially important because one or both contacting bodies are highly compliant. This also means that relatively low contact pressures may lead to finite deformations of the contacting bodies. The corresponding effects have so far attracted little attention, and a study of those effects is pursued in this work.

Modelling of an EHL problem involves description of the fluid part, of the solid part and of the elastohydrodynamic coupling [11, 12]. The fluid part is conveniently modelled using the classical Reynolds equation. In the classical EHL theory, the solid part is modelled using the linear elasticity framework. Furthermore, the elasticity problem is usually formulated for a half-space for which specialized solution techniques are available. While both assumptions (linear elasticity and half-space approximation) are fully adequate for hard-EHL problems, this is not necessarily so in the case of soft-EHL problems due to geometrical and material nonlinearities that are associated with the finite deformations and finite configuration changes.

The elastohydrodynamic coupling involves the solid-to-fluid coupling (lubricant film thickness depends on the deformation of the body) and the fluid-to-solid coupling (the hydrodynamic pressure and the shear stress are applied to the body as a surface traction). However, the Reynolds equation is formulated in an Eulerian frame on the contact boundary of the solid, and this introduces an additional coupling [13] due to the finite configuration changes (the domain on which the Reynolds equation is solved depends on the deformation of the solid).

A possible approach to modelling of the soft-EHL problems is to use the classical EHL theory, i.e., to neglect all the finite-deformation effects mentioned above. For instance, de Vicente et al. [7] applied the classical EHL solver to simulate an elastomeric point contact and derived a regression equation for the friction coefficient by fitting the corresponding numerical solutions. Their numerical solution was compared to experimental measurements, and a very good agreement was observed [7, 14]. The experiments involved moderately large deformations as the ratio of the Hertzian contact

radius to the ball radius was 0.17. Quite surprisingly, as shown in the present paper, the regression equation of [7] agrees very well with the predictions of the present fully nonlinear model also for much higher loads (and thus for much larger deformations) for which the ratio of the Hertzian contact radius to the ball radius exceeds 0.3. Despite the good agreement in terms of the friction coefficient, the local values of film thickness and hydrodynamic pressure do not exhibit such a good agreement. Furthermore, some notions, such as the central film thickness, are no longer well defined once finite configuration changes are involved.

The elastic half-space approximation is a feasible approach for point and line contacts. If more complex geometry is involved, computational techniques such as the finite element method are needed to reliably determine the contact pressure. In early works, the linear elasticity framework combined with the finite element method was adopted in the modelling of soft-EHL problems, for instance, in [15, 16] in the context of reciprocating seals.

Finite deformation effects are partially taken into account in a more advanced approach in which the contact pressure is computed for a fully nonlinear frictionless contact problem, typically using the finite-element method. Subsequently, a (linear) influence coefficient matrix is obtained from off-line finite-element computations, e.g., employing a nodal perturbation technique, and this matrix is used in the EHL solver [17, 18]. In other words, in this approach, the nonlinear behaviour of the deforming solid is linearized at the deformed state determined by solving the contact problem. As a drawback, the friction stresses are neglected in this approach, as they are not known a priori and thus cannot be included in the contact analysis.

A general, fully-coupled nonlinear framework for modelling of soft-EHL problems in the finite deformation regime has been developed in [13, 19]. In that approach, deformation of the solid is modelled using the finite element method which allows to consistently treat material nonlinearities and finite configuration changes. The fluid part is also solved using the finite element method. The Reynolds equation is formulated on the deforming contact surface of the solid. As a result, the corresponding domain and its discretization are not known a priori. In particular, the finite element mesh is defined by the deforming mesh of the contact surface of the solid. All the elastohydrodynamic couplings mentioned above are fully accounted for, and the problem is solved simultaneously for all unknowns, i.e., for displacements of the solid, lubricant pressures, and possibly other quantities involved in the model, using the Newton method (monolithic approach). Recently, the model has been

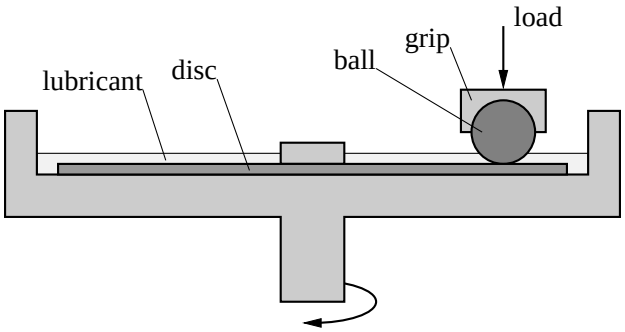

Figure 1: Schematic of the ball-on-disc tribometer.

combined with the mass-conserving cavitation model, and the formulation has been extended to three-dimensional problems [20].

In the present paper, the general framework [13, 19, 20] is further developed and is applied to study finite-deformation effects in soft-EHL. Specifically, in Section 3, the formulation is extended to the case of non-planar contact, and the related issue of the choice of the domain on which the Reynolds equation is solved is discussed in detail. Subsequently, in Section 4, the finite-deformation effects are studied for a two-dimensional problem of a rigid cylinder sliding against a coated layer and for a three-dimensional problem of an elastic ball sliding against a rigid plane.

The main focus of this work is on development of computational tools for modelling of soft-EHL problems in the finite deformation regime. However, in parallel, we have developed an experimental test rig suitable for examining pure-sliding lubricated contact of compliant elastomeric balls under high loads. The test rig and sample results are described in Section 2, and the measured friction coefficients are compared to the theoretical predictions.

2. Friction measurements at high contact loads

2.1. Experimental method

Friction measurements were made using a home-made ball-on-disc tribometer shown schematically in Fig. 1. In this tribometer, an elastomeric ball is placed in a grip and is loaded by a normal force against a rotating flat disc. The tribometer has been designed such that testing at relatively high normal loads is possible. The normal load is controlled by attaching a mass (dead load) to an otherwise balanced arm supporting the ball grip.

Table 1: Viscosity of the lubricants at the test temperature.

Fluid	Viscosity at 25°C [Pa s]
Distilled water	0.000891
OM 10	0.00942
OM 50	0.0493
OM 300	0.3395
OM 3000	2.735

The disc is clamped to a supporting disc and both are placed in a container. A thin lubricant layer is continuously maintained on the disc surface to ensure proper lubrication conditions. The setup allows testing of steady-state lubrication in pure sliding only, and the sliding speed is adjusted by changing the angular speed of the supporting disc and the radial position of the ball. Friction force is measured by a load cell attached to the ball grip.

Nitrile butadiene rubber (NBR) balls of radius $R = 10.7$ mm were used in the present study. The Young's modulus was estimated as $E = 3.5$ MPa by performing instrumented indentation and by fitting the resulting force–displacement response using the Hertzian contact theory. However, the material exhibits hysteretic effects even at low loading rates, hence the estimated Young's modulus is regarded approximate. A polished low-carbon steel disc was used as a counter surface. Due to a high difference in elastic stiffness, the steel disc can be assumed rigid.

The root-mean-square roughness R_q was measured using the Hommel-Etamic T8000 Nanoscan scanning profilometer: R_q of the steel disc was 0.17 μm and R_q of the rubber balls was 1.30 μm. In the latter case, the roughness was measured on the mould used for producing the balls, as the rubber is too compliant for stylus profilometry.

Distilled water and four silicone oils (Polsil OM 10, OM 50, OM 300 and OM 3000 produced by Silikony Polskie, Poland) were used as the lubricants. Polsil OM fluids are linear, non-reactive, unmodified polydimethylsiloxanes. They differ in their degree of polymerization and consequently in viscosity. The dynamic viscosity η at the test temperature of 25°C was measured using the Brookfield HADV-III Ultra viscometer with cone/plate configuration and is provided in Table 1.

The disc was driven with a constant angular velocity which resulted in the sliding speed V between 62 and 690 mm/s for the fixed position of the ball with respect to the axis of rotation. The corresponding radius of the

sliding path was 42 mm.

The tests were carried out at the normal load W equal to 0.25, 0.98, 5.13 and 19.3 N. This range corresponds to the dimensionless load $\overline{W}$, see Eq. (1), varying between 0.00023 and 0.018. The maximum dimensionless load is thus here more than four times higher than the highest load applied in [4] in a study of the influence of load on friction of lubricated soft contacts.

Adopting the Young's modulus of 3.5 MPa, the theoretical Hertzian contact radius a_{Hertz} varies between 0.75 mm for $W = 0.25$ N and 3.21 mm for $W = 19.34$ N, so that the corresponding ratio a_{Hertz}/R varies between 0.07 and 0.30. The magnitude of the load was thus sufficiently high to cause relatively large deformations of the ball.

For each lubricant and for each normal load, the test protocol was as follows. The steel disc was cleaned with acetone and clamped on the top of the supporting disc. The rubber ball was cleaned with ethanol and was placed in the grip and loaded against the steel disc with a chosen value of the normal load. The friction force was then measured in the whole range of sliding speeds at series, starting from the lowest one.

2.2. Experimental results and discussion

Figure 2 shows a log–log plot of the measured friction coefficient as a function of the product of the viscosity η and the entrainment speed U, where the entrainment speed is here equal to one half of the sliding speed, $U = V/2$. The results corresponding to a fixed load are denoted by markers of the same colour, and the results corresponding to a fixed lubricant are denoted by markers of the same shape, see the legend in Fig. 2.

It can be seen that the results corresponding to each load form a part of the classical Stribeck curve with a continuous transition between the results corresponding to the lubricants of different viscosity. At high values of $U\eta$, the dependence of the friction coefficient on $U\eta$ appears approximately linear on the log–log plot which indicates that the contact operates in the hydrodynamic lubrication regime. At low values of $U\eta$, the contact operates in the mixed lubrication regime and the friction coefficient increases with decreasing $U\eta$.

Considering the dependence on the load, it is apparent that the friction coefficient decreases with increasing load in the whole range of the examined values of $U\eta$.

Based on the predictions of the classical EHL theory, de Vicente et al. [7] have derived a regression equation for the friction coefficient in soft-EHL

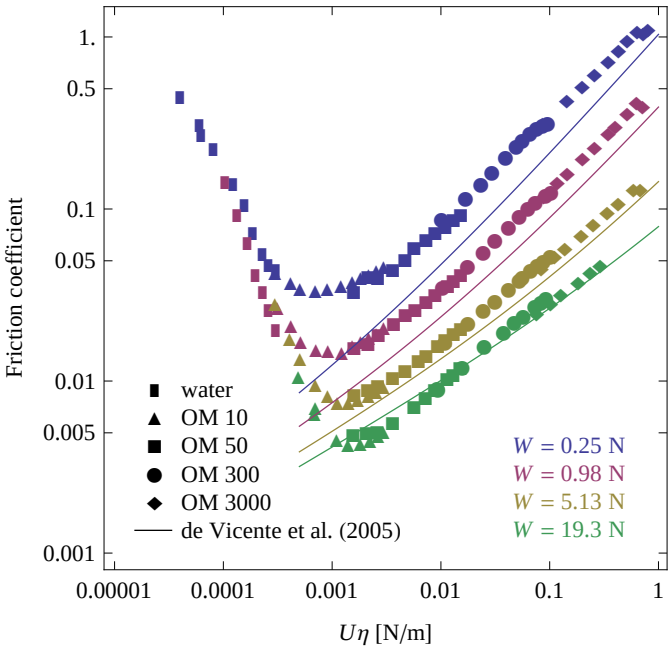

Figure 2: Friction coefficient as a function of the product of entrainment speed U and viscosity η for five lubricants and a range of loads W. Solid lines indicate the predictions of the regression equation (1) of de Vicente et al. [7].

contacts. According to this equation, the total friction coefficient, composed of the Couette and Poiseuille contributions, is given by

$$\mu_{\text{total}} = SRR\left(3.8\overline{U}^{0.71}\overline{W}^{-0.76} + 0.96\overline{U}^{0.36}\overline{W}^{-0.11}\right) \pm 1.46\overline{U}^{0.65}\overline{W}^{-0.70}, \quad (1)$$

where $\overline{U} = U\eta/(E'R')$ and $\overline{W} = W/(E'R'^2)$. Considering that the disc is flat and rigid, the reduced radius R' is here equal to R and the reduced modulus E' is equal to $2E/(1-\nu^2)$, where, assuming incompressibility, the Poisson's ratio ν is equal to 0.5. The first term in Eq. (1) describes the Couette contribution to friction, and SRR denotes the slide-roll ratio equal to 2 for pure sliding. The second term describes the Poiseuille contribution, the sign of which is negative for the ball and positive for the disc. In our experimental setup, the total friction force acting on the ball is measured, hence the minus sign in Eq. (1) applies.

The predictions of the regression equation (1) are included in Fig. 2. The agreement between the theoretical predictions and the experimental values corresponding to the hydrodynamic lubrication regime is reasonably good with the highest discrepancy reaching 30% at the lowest load. At the same time, the dependence of the friction coefficient on $U\eta$ (i.e., the slope on the log–log plot) and the dependence on the load are in a good agreement.

In Section 4.2, it is shown that the friction coefficient in the present soft-EHL point contact is not affected by finite deformations although the film thickness and pressure are clearly affected. Accordingly, the regression equation (1) is valid also at high loads. Thus, the comparison of the experimental results with the predictions of the fully nonlinear model discussed below would look exactly the same as the comparison presented in Fig. 2, and such comparison is omitted.

The discrepancy between the measured friction coefficients and the theoretical predictions, see Fig. 2, may partially result from viscoelasticity of the rubber material used in the present study. Note that, in the theoretical model, it is assumed that the material is elastic so that the possible viscoelastic effects cannot be captured. At the same time, these effects may influence the actual deformation pattern and contact pressure, and, as a result, the lubrication conditions. It is also noted that the discrepancy is not caused by a possible inaccuracy of the estimated Young's modulus: it has been checked that the agreement of theoretical and experimental results cannot be significantly improved by varying the Young's modulus.

3. Computational model of a fully coupled soft-EHL problem

Two main assumptions are adopted in the present computational model. Firstly, it is assumed that only one of the contacting bodies is deformable, while the other one is rigid. This corresponds to a typical situation in which a compliant elastomeric body interacts with a metallic or ceramic body. The large difference of elastic moduli justifies then the rigid-body assumption. A hyperelastic model is adopted to describe material behaviour of the deformable body subjected to finite deformations. Consideration of viscoelastic effects is, in principle, possible but is not pursued here.

Secondly, the model and its implementation are currently restricted to steady-state conditions. As discussed in Section 3.2, the Reynolds equation is formulated and solved on a domain that is not known a priori and constitutes a part of the solution of the coupled EHL problem. For a transient lubrication problem, this domain (and its finite element discretization) would thus vary in time. Extension of the model to transient problems would require consideration of advective terms related to mesh movement.

The formulation presented below follows our earlier work on the soft-EHL problems [13, 19] and on the mass-conserving cavitation model [20]. In the present paper, the formulation is further developed for the case of non-planar contact. In particular, the related issue of the choice of the domain on which the Reynolds equation is solved is discussed in detail. The corresponding effects are also studied in the numerical example of Section 4.1.

3.1. Deformation subproblem

Following the standard approach, two configurations of the solid are introduced: the reference configuration Ω and the deformed configuration ω, the former is assumed to be a stress-free initial configuration. The deformation from Ω to ω is described by a continuous mapping $\boldsymbol{x} = \boldsymbol{\varphi}(\boldsymbol{X})$, where $\boldsymbol{X} \in \Omega$ and $\boldsymbol{x} \in \omega$. The boundary $\partial\Omega$ is divided into non-overlapping parts: Γ_d with prescribed displacement, Γ_t with prescribed traction, and Γ_l with contact interaction in the hydrodynamic lubrication regime. For simplicity, in the following, it is assumed that the traction prescribed on Γ_t is equal to zero so that it does not appear in the formulation.

The equation of mechanical equilibrium, written in the reference configuration, reads

$$\mathrm{Div}\boldsymbol{P} = \boldsymbol{0} \quad \text{in } \Omega, \tag{2}$$

where $\boldsymbol{P}$ is the first Piola–Kirchhoff tensor, and Div denotes the divergence in the reference configuration. For a hyperelastic body, the first Piola–Kirchhoff tensor is specified by the elastic strain energy function $W(\boldsymbol{F})$,

$$\boldsymbol{P} = \frac{\partial W}{\partial \boldsymbol{F}}, \tag{3}$$

where $\boldsymbol{F} = \partial\boldsymbol{\varphi}/\partial\boldsymbol{X} = \mathrm{Grad}\boldsymbol{\varphi}$ is the deformation gradient.

The weak form of the equilibrium equation (2), i.e., the virtual work principle, is obtained using the standard procedure, and reads

$$\int_\Omega \boldsymbol{P} \cdot \mathrm{Grad}\delta\boldsymbol{\varphi}\,\mathrm{d}\Omega - \int_{\Gamma_\mathrm{l}} \boldsymbol{T} \cdot \delta\boldsymbol{\varphi}\,\mathrm{d}\Gamma = 0, \tag{4}$$

where $\delta\boldsymbol{\varphi}$ is the virtual displacement (test function) that vanishes on Γ_d, and $\boldsymbol{T}$ is the nominal traction resulting from the contact interaction on the lubricated boundary Γ_l. As discussed below, the Reynolds equation, which governs the lubrication subproblem, is formulated in the deformed configuration, and so is the corresponding traction exerted on the solid. Accordingly, the surface traction term in (4) is transformed to the deformed configuration

$$\int_\Omega \boldsymbol{P} \cdot \mathrm{Grad}\delta\boldsymbol{\varphi}\,\mathrm{d}\Omega - \int_{\gamma_\mathrm{l}} \boldsymbol{t} \cdot \delta\boldsymbol{\varphi}\,\mathrm{d}\gamma = 0, \tag{5}$$

where $\boldsymbol{t}$ is the spatial traction, i.e., one referred to the unit area in the deformed configuration γ_l.

3.2. Lubrication subproblem

Flow of lubricant in a thin film between two contacting surfaces is commonly described using the Reynolds equation which is obtained by integrating the Navier–Stokes equation over the thickness of the fluid film [11]. As a result, the dimension of the problem is reduced. The Reynolds equation is thus formulated on the contact surface, and a two-dimensional Reynolds equation is obtained in a general three-dimensional case.

The Reynolds equation relies on the assumption that the film thickness is small compared to the other dimensions of the lubrication domain. The two contacting surfaces are thus assumed to approximately coincide and are represented by a single surface S. In the present context of finite deformations, that assumption needs some care, as explained below.

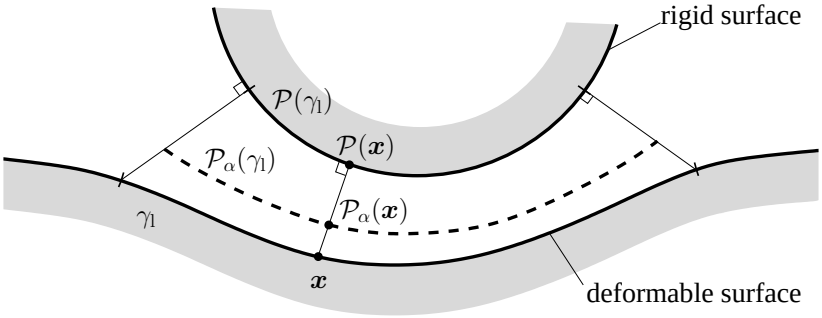

Figure 3: Construction of the domain on which the Reynolds equation is formulated: γ_l is the lubricated boundary in the current configuration, $\mathcal{P}(\gamma_l)$ its projection on the rigid counter-surface, and $\mathcal{P}_\alpha(\gamma_l)$ an intermediate surface.

Following the usual approach in contact mechanics [21], we assume that the contact pair is formed by the deformed boundary γ_l and its projection on the rigid surface denoted by $\mathcal{P}(\gamma_l)$. Now, there is some freedom is choosing the domain on which the Reynolds equation is formulated. One can assume $S = \gamma_l$, or $S = \mathcal{P}(\gamma_l)$, or more generally $S = \mathcal{P}_\alpha(\gamma_l)$, where $\mathcal{P}_\alpha(\gamma_l)$ is an intermediate surface with parameter α defining its position between γ_l and $\mathcal{P}(\gamma_l)$, such that

$$\mathcal{P}_\alpha(\boldsymbol{x}) = \alpha\boldsymbol{x} + (1-\alpha)\mathcal{P}(\boldsymbol{x}) \tag{6}$$

for $\boldsymbol{x} \in \gamma_l$, see Fig. 3. The value of α may be adopted between $\alpha = 0$, which corresponds to $S = \mathcal{P}(\gamma_l)$, and $\alpha = 1$, which corresponds to $S = \gamma_l$.

Considering that the lubricant film thickness is very small in typical conditions, the choice of the position of S between γ_l and $\mathcal{P}(\gamma_l)$ should not noticeably affect the results. Only in the inlet and outlet zones, the film thickness may be relatively large. However, the hydrodynamic pressure buildup is mostly concentrated in the zones where the film thickness is small. The related effects are studied in Section 4.1 where it is shown that indeed the results do not significantly depend on the choice of the position of S, while the computational scheme appears more robust for $S = \mathcal{P}(\gamma_l)$.

Hydrodynamic lubrication is typically accompanied by cavitation, and adequate treatment of this phenomenon constitutes an important part of the corresponding computational schemes. Whenever cavitation occurs, the lubrication domain S is divided into the full-film region S_f and the cavitated region S_c. With reference to the soft EHL problems, which are typically characterized by relatively low hydrodynamic pressures, the lubricant is assumed

incompressible in the full-film region.

Presented below is the formulation of the Reynolds equation with a mass-conserving cavitation model developed recently in [20]. In general terms, the present cavitation model is equivalent to the Elrod–Adams model [22] and, in particular, to its more recent formulations [23, 24], though it exhibits some subtle differences concerning the continuum formulation and finite element treatment, see [20]. In particular, the present two-field formulation proves particularly suitable for the hanging-node mesh refinement technique used in the example of Section 4.2.

The mass-balance equation in steady-state conditions reads

$$\operatorname{div}_S(\bar{\varrho}\boldsymbol{q}) = 0 \quad \text{on } S, \tag{7}$$

where $\boldsymbol{q}$ is the volumetric flux, $\bar{\varrho} = \varrho/\varrho_0$ the relative density, and ϱ_0 the density of the intact fluid. Divergence is here evaluated on S hence the relevant surface divergence operator $\operatorname{div}_S(\cdot)$ is employed, see Appendix A.

The flow in the full-film region S_f is governed by the classical Reynolds equation, and the flux $\boldsymbol{q}$ is given by

$$\boldsymbol{q} = \boldsymbol{u}h - \frac{h^3}{12\eta}\operatorname{grad}_S p \quad \text{on } S_\mathrm{f}, \tag{8}$$

where p is the pressure, h the film thickness, $\boldsymbol{u} = \frac{1}{2}(\boldsymbol{u}_1 + \boldsymbol{u}_2)$ the average velocity of the surfaces, η the lubricant viscosity, and $\operatorname{grad}_S(\cdot)$ denotes the surface gradient operator, see Appendix A. In the cavitated region S_c, the flux is only due to the Couette-like flow, thus

$$\boldsymbol{q} = \boldsymbol{u}h \quad \text{on } S_\mathrm{c}. \tag{9}$$

Cavitation occurs whenever the pressure drops to the cavitation pressure p_cav, and the pressure is constant and equal to the cavitation pressure $p = p_\mathrm{cav}$ in the cavitated region S_c. For simplicity, the cavitation pressure is assumed to be equal to zero, $p_\mathrm{cav} = 0$. At the same time, the density of the cavitating fluid is lower than the (constant) density ϱ_0 of the intact fluid. This can be compactly written in the form of the following complementarity conditions,

$$p \geq 0, \quad \bar{\varrho} - 1 \leq 0, \quad p(\bar{\varrho} - 1) = 0 \quad \text{on } S. \tag{10}$$

The mass-balance equation (7) is accompanied by the continuity condition that enforces the mass balance on the cavitation boundary Σ,

$$(\bar{\varrho}^+\boldsymbol{q}^+ - \bar{\varrho}^-\boldsymbol{q}^-) \cdot \boldsymbol{\nu} = 0 \quad \text{on } \Sigma, \tag{11}$$

where $\boldsymbol{\nu}$ is the unit vector tangent to S and normal to Σ, and oriented outwards from S_c. The superscripts $+$ and $-$ denote the limit values of the corresponding quantities as Σ is approached from the full-film and cavitated side, respectively.

Finite element formulation of the lubrication and cavitation subproblem is based on the weak form of the governing equations. Detailed derivation of the weak form is given in [20]. In brief, the mass-balance equation (7) is multiplied by a test function δp and integrated over the lubrication domain S. The integral over S is then split into two parts corresponding to S_f and S_c, the pressure-gradient term is integrated by parts within S_f, and condition (11) of mass-flux balance at the cavitation boundary Σ is used. As a result, the following weak form of the mass-balance equation in obtained

$$\int_S \left[\mathrm{grad}_S \delta p \cdot \left(\frac{\bar{\varrho} h^3}{12\eta} \mathrm{grad}_S p \right) + \delta p \, \mathrm{div}_S \left(\bar{\varrho} \boldsymbol{u} h \right) \right] \mathrm{d}S + \int_\Sigma \delta p (\bar{\varrho}^+ - \bar{\varrho}^-) h \boldsymbol{u} \cdot \boldsymbol{\nu} \, \mathrm{d}\Sigma \;=\; 0, \tag{12}$$

where $\delta p = 0$ on ∂S in view of the Dirichlet boundary condition $p = p^*$ prescribed on ∂S.

The last term in Eq. (12) is related to discontinuity of $\bar{\varrho}$ on the cavitation boundary Σ (note that the jump of density at the reformation boundary is a typical feature of the present cavitation model). Integration over an unknown cavitation boundary Σ would be an undesired feature from the point of view of computational treatment. However, this term vanishes once a *continuous* finite element approximation is introduced, see [20]. As a result, the jump of density is approximated by a continuous function with a high gradient at the reformation boundary.

In the mixed formulation developed in [20], both the pressure p and the relative density $\bar{\varrho}$ are kept as two independent variables and the complementarity conditions (10) are enforced using a non-smooth constraint function. Actually, for convenience, the relative density $\bar{\varrho}$ is replaced by the void fraction $\lambda = 1 - \bar{\varrho}$, for which the complementarity conditions take the standard form

$$p \geq 0, \quad \lambda \geq 0, \quad p\lambda = 0 \quad \text{on } S. \tag{13}$$

These are equivalently enforced using the constraint function $C(p, \lambda)$,

$$C(p, \lambda) = 0 \quad \text{on } S, \tag{14}$$

where

$$C(p,\lambda) = \lambda - \max(0, \lambda - \epsilon p), \quad \epsilon > 0. \tag{15}$$

The weak form of the constraint equation (14) is obtained by multiplying it by the test function $\delta\lambda$ and integrating over S, thus

$$\int_S \delta\lambda \, C(p,\lambda) \, \mathrm{d}S = 0. \tag{16}$$

The details concerning the finite element treatment of the lubrication and cavitation subproblem governed by the weak forms (12) and (16) are provided in [20], and only the most important issues are briefly commented below. Firstly, stable schemes have been obtained only for the nodal quadrature of the constraint equation (16). The resulting computational scheme becomes then equivalent to the single-field formulation of Hajjam and Bonenau [23]. However, in some situations, the present two-field formulation appears beneficial, see [20]. Secondly, application of an upwind scheme is necessary in order to adequately treat the advection equation in the cavitated region, and the streamline diffusion method [25] is adopted for that purpose. Finally, the contribution of the relative density $\bar{\varrho}$ in the Poiseuille term in Eq. (12) is neglected in practical computations. The lubrication subproblem is then transformed to a linear complementarity problem (LCP), cf. [24]. As thoroughly discussed in [20], this improves the robustness of the computational scheme, while the associated loss in accuracy is negligible.

3.3. Coupling of the deformation and lubrication subproblems

The essence of the elastohydrodynamic lubrication regime is in the strong coupling of the two subproblems involved. Firstly, the lubricant film thickness h depends on the deformation of the solid, thus

$$h = h(\boldsymbol{\varphi}), \tag{17}$$

where $\boldsymbol{\varphi}$ is governed by the virtual work principle (5) of the deformation subproblem. In the present formulation, the local film thickness h is defined by the projection algorithm, illustrated in Fig. 3, that defines the specific geometrical dependence of h on $\boldsymbol{\varphi}$.

Secondly, the surface traction $\boldsymbol{t}$, which constitutes the loading applied to the solid, see Eq. (5), depends on the hydrodynamic pressure p and its gradient, thus

$$\boldsymbol{t} = \boldsymbol{t}(p, \mathrm{grad}_S p), \tag{18}$$

where p is governed by the Reynolds equation (12). Specifically, the parabolic velocity profile predicted by the Reynolds equation results in the following expression for the surface traction,

$$\boldsymbol{t} = -p\boldsymbol{n} + \frac{\eta}{h}\,\Delta\boldsymbol{u} - \frac{h}{2}\,\mathrm{grad}_S p. \tag{19}$$

The first term describes the normal traction due to the hydrodynamic pressure p, and $\boldsymbol{n}$ is the outer normal to the lubricated boundary γ_l in the deformed configuration. The second term is the shear (friction) stress due to the Couette flow associated with the tangential relative velocity $\Delta\boldsymbol{u}$. The last term is the shear stress due to the Poiseuille flow induced by the pressure gradient. It is well known that Eq. (19) may overpredict the shear stresses in the cavitation zone, see [7]. As a remedy, the Couette shear stress in Eq. (19) can be multiplied by a term $(1-\lambda)$ so that the shear stress is reduced in the cavitation zone (for $\lambda > 0$). However, as shown in Section 4.1, this has a negligible effect on the predicted overall friction coefficient.

Thirdly, finite deformations and the associated finite configuration changes introduce yet another coupling. As discussed in Section 3.2, the Reynolds equation is formulated and solved on the surface S which is defined by the projection of the deformed lubricated boundary γ_l on the rigid countersurface, see Fig. 3. The surface S is not known a priori and constitutes a part of the solution of the problem. In practical terms, upon finite element discretization, the positions of the nodes of the finite element mesh used to solve the Reynolds equation (12) depend on the deformation of the solid. The additional coupling described above is not present in the small-strain regime that is typically considered in the EHL theory.

Following the approach developed in [13, 19], the present coupled problem is solved monolithically for all unknowns. The basic unknowns of the solid deformation subproblem are the displacements, and the corresponding discrete finite-element equations are derived by assuming that the surface traction $\boldsymbol{t}$ is given. Likewise, the basic unknowns of the lubrication subproblem are the pressure p and the void fraction λ, and the corresponding discrete finite-element equations are derived by assuming that the surface S, the film thickness h, and the average velocity $\boldsymbol{u}$ are given. The two sets of nonlinear equations are then solved simultaneously using the Newton method. The tangent matrix needed in the Newton method is obtained by linearization of the finite-element equations, and here all the couplings discussed above are fully accounted for.

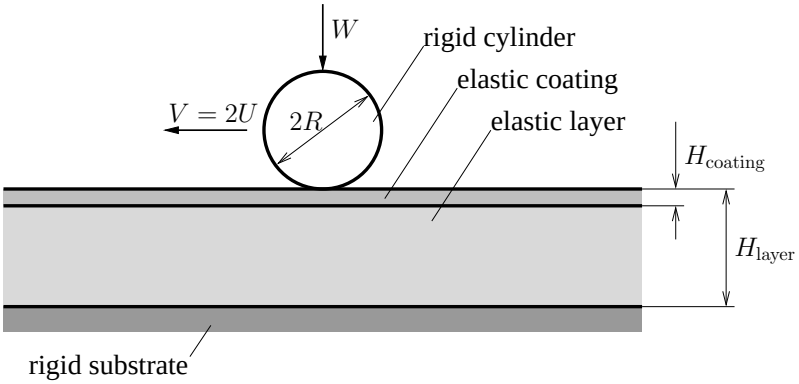

Figure 4: Rigid cylinder sliding against a coated layer.

The present finite-element implementation and the computations have been performed using the *AceGen/AceFEM* system [26]. Details of the finite-element implementation of the individual subproblems are omitted here, as the solid part is standard, and the treatment of the fluid part is described in detail in [20]. As mentioned above, the coupling of the two subproblems is fully accounted for while deriving the tangent matrix for the Newton method. The relevant dependencies and their derivatives are efficiently derived and implemented using the automatic differentiation technique available in *AceGen*.

4. Numerical examples

4.1. Rigid cylinder sliding against a coated layer

A two-dimensional problem of a rigid cylinder sliding against a soft layer with a harder thin coating is considered first, see Fig. 4. Both the layer and the coating are assumed elastic (hyperelastic), and hysteretic effects typical for elastomeric materials are thus not included in the analysis. The problem is analyzed in a coordinate system attached to the cylinder.

Geometrical, material and process parameters are summarized in Table 2. The hyperelastic behaviour of the layer and coating is governed by an elastic strain energy function of neo-Hookean type. The value of the Poisson's ratio equal to 0.49 corresponds to a nearly incompressible material behaviour. In order to avoid volumetric locking effects, a four-node quadrilateral plane-strain element employing Taylor expansion of shape functions, volumetric–

Table 2: Coated layer: geometrical, material and process parameters.

Cylinder radius, R	5 mm
Total thickness of the layer, H_{layer}	10 mm
Thickness of the coating, H_{coating}	1 mm
Young's modulus of the layer, E_{layer}	0.1 MPa
Young's modulus of the coating, E_{coating}	1 MPa
Poisson's ratio, $\nu_{\text{layer}} = \nu_{\text{coating}}$	0.49
Lubricant viscosity, η	0.1×10^{-6} MPa s
Nominal entrainment speed, $U = V/2$	10–10^4 mm/s
Load, W	0.1–1 N/mm

deviatoric split of deformation gradient and selective integration [27] is used for finite element discretization of the solid part.

It is assumed that the layer is bonded to a rigid substrate, hence the displacements at the bottom of the layer are fully constrained. A finite length of the layer (100 mm) is included in the analysis and the horizontal displacements are constrained at the ends. The central part of the top surface (spanning 13 mm) has been adopted as the lubricated part of the boundary, Γ_{l}. This choice is somewhat arbitrary and is dictated by two factors. Firstly, the length of Γ_{l} must be sufficiently large so that the pressure buildup in the inlet zone is not affected, and the fully-flooded conditions are maintained. Secondly, it cannot be exceedingly large so that the projected domain $\mathcal{P}(\gamma_{\text{l}})$ does not get degenerated at high loading (see, for instance, the deformation pattern in Fig. 5d below). At the ends of the lubricated boundary, the hydrodynamic pressure is prescribed as $p = 0$.

The sliding speed $\boldsymbol{V}$ defines the *nominal* entrainment speed $\boldsymbol{U}$ which is equal to one-half of the sliding speed, $\boldsymbol{U} = \boldsymbol{V}/2$. However, due to finite deformations, the local velocity $\boldsymbol{v}$ of the points of the layer is equal to $\boldsymbol{v} = \boldsymbol{F}\boldsymbol{V}$, in steady-state conditions, where $\boldsymbol{F}$ is the deformation gradient. Accordingly, the average velocity $\boldsymbol{u} = \boldsymbol{v}/2$, which appears in the Reynolds equation, and the local relative (sliding) velocity $\Delta\boldsymbol{u} = \boldsymbol{v}$, which is needed to compute the friction stress, are not constant and depend on the solution through $\boldsymbol{F}$. Actually, for consistency, both $\boldsymbol{u}$ and $\Delta\boldsymbol{u}$ are projected on the surface S, and the corresponding tangential components are used in the Reynolds equation. The range of nominal entrainment speeds specified in Table 2 corresponds to $U\eta$ varying between 0.001 and 1 N/m.

The deformed finite element mesh is shown in Fig. 5. Large deformations

of the layer are clearly visible, particularly at higher loads. Note that a coarse mesh is shown in Fig. 5 for better visualization. The actual computations have been carried out using a much finer mesh with the elements at least four times smaller than those shown in Fig. 5.

Figure 5 corresponds to the highest sliding speed considered ($U\eta = 1$ N/m), hence the lubricant film thickness is large, and the gap between the layer and the cylinder is clearly visible. At such a high sliding speed and for a small load (e.g., for $W = 0.1$ N/mm), the ratio of the film thickness to the contact length is relatively large so that the Reynolds equation may no longer be applicable. Nevertheless, having the above limitations in mind, for the sake of completeness, the corresponding results are reported below along with the other results.

It can be seen in Fig. 5 that, for a high load, the ridge at the inlet is higher than that at the outlet, which is due to friction forces. At lower sliding speeds and lower loads, friction forces are smaller and this effect is less pronounced.

Film thickness and pressure profiles are illustrated in Fig. 6 for two representative sliding speeds. The position is measured along the surface in the deformed configuration, and the zero value corresponds to the point lying below the centre of the cylinder. In the film thickness profile, a characteristic ridge is formed at the trailing edge of the contact zone. The ridge is sharp for low $U\eta$ and gets more rounded for increasing $U\eta$.

To illustrate the finite deformation effects, the results obtained using a geometrically linear model are also included in Fig. 6 (dashed lines). In that model the configuration changes are neglected and the material behaviour is governed by linear elasticity. The difference with respect to the present fully nonlinear model is significant even at lower loads.

Figure 7 shows the predicted friction coefficient as a function of the sliding speed (expressed by $U\eta$) and load W. The dependence of the friction coefficient on $U\eta$ is approximately linear on the log–log plot. As discussed in Section 3.3, the shear stresses in the cavitation zone are overpredicted by Eq. (19). The solid lines in Fig. 7 correspond to Eq. (19), and the dashed lines correspond the formulation in which the Couette shear stresses in the cavitation region are reduced by the factor $(1 - \lambda)$. The effect is negligible.

Finally, we study the effect of the position of the surface S on which the Reynolds equation is solved, see Fig. 3. It is seen in Fig. 8 that the solution depends weakly on parameter α specifying the position of S between the lubricated boundary γ_l and its projection on the rigid countersurface, $\mathcal{P}(\gamma_l)$. For $U\eta = 0.1$ N/m, the effect is hardly visible, and it is negligible for lower

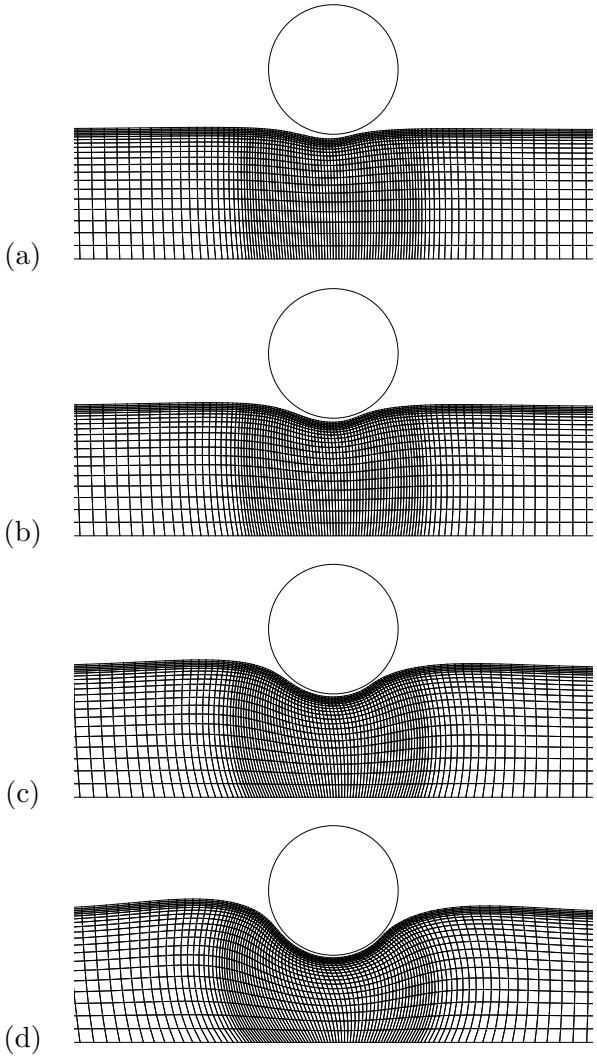

Figure 5: Detail of the deformed finite element mesh for: (a) $W = 0.1$ N/mm, (b) $W = 0.2$ N/mm, (c) $W = 0.5$ N/mm, (d) $W = 1$ N/mm. A much finer mesh is used in the actual computations (see text).

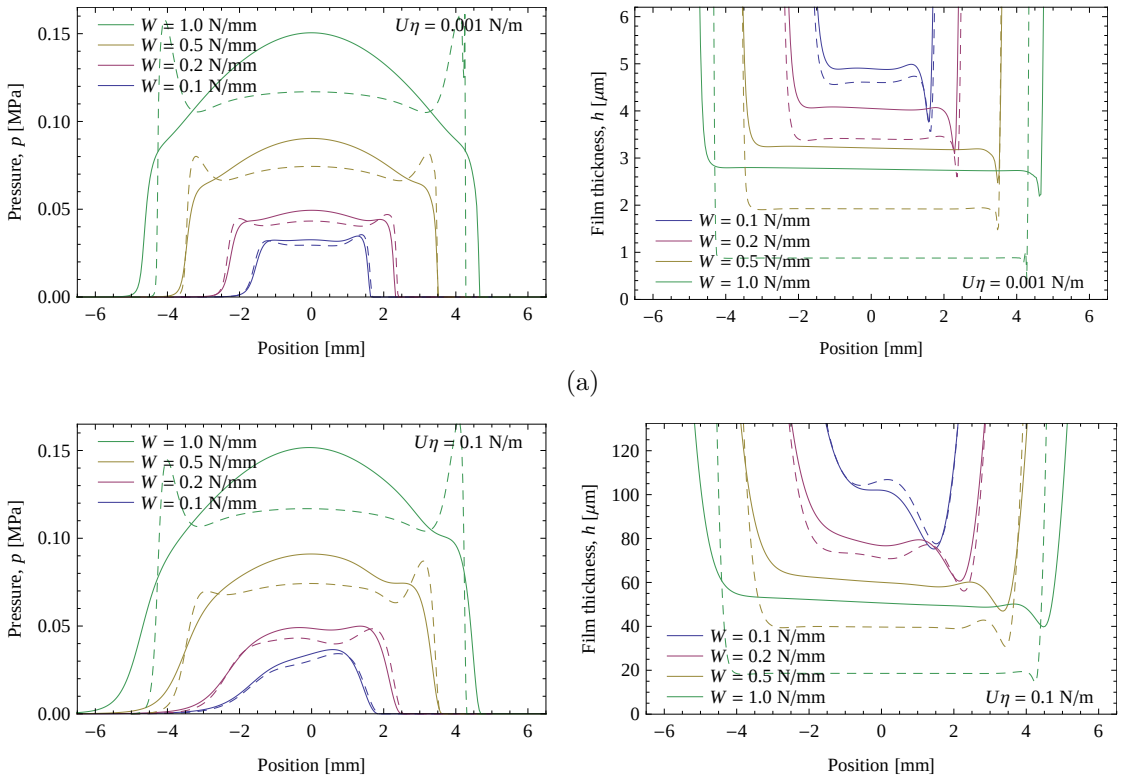

Figure 6: Hydrodynamic pressure p (left) and film thickness h (right) corresponding to different loads and nominal entrainment speeds: (a) $U\eta = 0.001$ N/m, (b) $U\eta = 0.1$ N/m. Dashed lines indicate the results of the geometrically linear model.

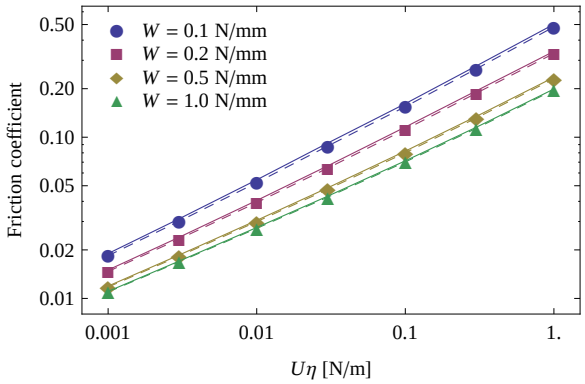

Figure 7: Friction coefficient as a function of $U\eta$. Dashed lines correspond to the Couette shear stress in Eq. (19) reduced by the factor $(1 - \lambda)$.

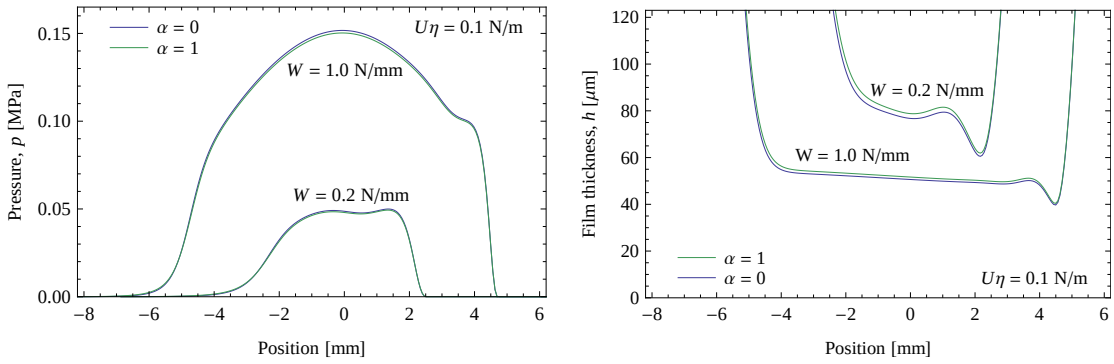

(a)

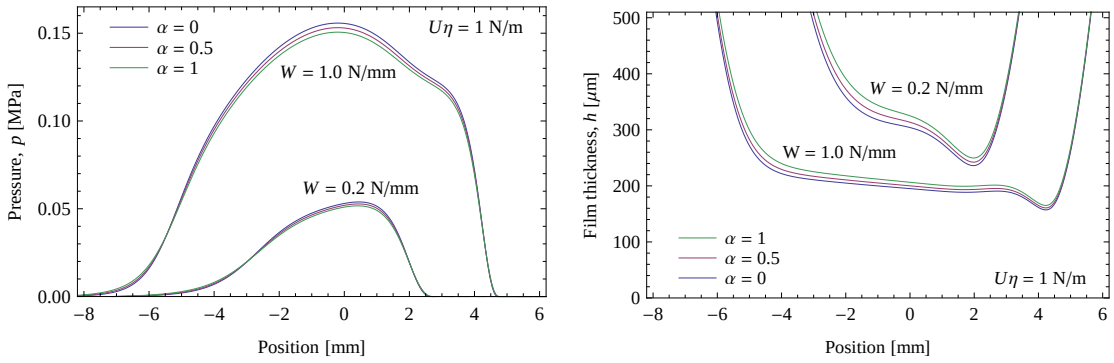

(b)

Figure 8: Effect of parameter α specifying the position of the surface S between γ_1 and $\mathcal{P}(\gamma_1)$: pressure p (left) and film thickness h (right) for (a) $U\eta = 0.1$ N/m and (b) $U\eta = 1.$ N/m ($W = 1$ N/mm).

sliding speeds (not shown).

At the same time, it has been observed that the Newton-based solution scheme behaves better for $\alpha = 0$ than for $\alpha = 1$. Specifically, in more severe lubrication conditions (i.e., for higher loads and for lower sliding speeds), the Newton scheme did not converge for $\alpha = 1$, while such problems have not been encountered for $\alpha = 0$. It is thus concluded that the choice of $\alpha = 0$, i.e., $S = \mathcal{P}(\gamma_1)$, is preferable, and that scheme is used in the 3D example that follows.

4.2. Elastic ball sliding against a rigid plane

As the second example, we consider a hyperelastic ball sliding against a rigid plane in steady-state conditions. The setup corresponds to that studied

Table 3: Elastic ball: geometrical, material and process parameters.

Ball radius, R	9.25 mm
Young's modulus, E	2.4 MPa
Poisson's ratio, ν	0.49
Lubricant viscosity, η	0.78×10^{-6} MPa s
Entrainment speed, $U = V/2$	10^2–10^5 mm/s
Load, W	1–40 N

experimentally in Section 2, except that the curvature of the sliding path and the related spin are neglected here. However, the geometrical and material parameters are different, as they are identical to those used in the soft-EHL example in [20, Sect. 4.5], see Table 3. Note that the highest entrainment speeds considered (reaching 10^5 mm/s) are clearly unrealistic, but they are included in the analysis for completeness. The lowest entrainment speed $U = 100$ mm/s corresponds to $\overline{U} = 1.33\times10^{-6}$, and this value corresponds to $U\eta = 0.027$ N/m in the experiment in Section 2. Simulation of lower entrainment speeds is possible, see [20], but a finer mesh is then needed. The dimensionless load $\overline{W}$ is here between 0.0018 and 0.074, and this approximately corresponds to the range of dimensionless loads (between 0.00024 and 0.018) examined in Section 2.

The finite element mesh used in the computations is shown in Fig. 9a. Displacements are fully constrained at the top surface, and the symmetry with respect to the vertical plane $y = 0$ aligned with the direction of sliding is exploited in order to reduce the size of the problem. Note that the mesh is significantly refined in the vicinity of the contact zone and, in particular, at the trailing edge. This is needed to avoid spurious oscillations in more severe lubrication conditions, see [19]. The Dirichlet boundary condition for the Reynolds equation, $p = 0$, is prescribed far from the contact zone, which corresponds to the fully flooded condition.

The finite element mesh comprises almost 100,000 hexahedral 8-node F-bar elements [28], and the total of 480,181 unknowns including nodal displacements in the body, pressures and void fractions on the lubricated contact surface and the Lagrange multipliers associated with the hanging-node mesh refinement technique.

The deformed configuration corresponding to the load $W = 40$ N is shown in Fig. 9b, and the colour map indicates the σ_{zz} component of the Cauchy stress. Finite deformations of the ball are clearly visible. At the load of 40

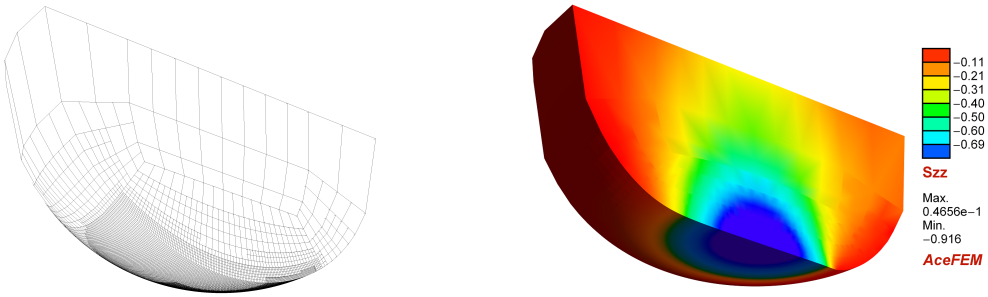

(a) (b)

Figure 9: Hyperelastic ball sliding against a rigid plane: (a) finite element mesh, (b) σ_{zz} component of the Cauchy stress (in MPa) in the deformed configuration at the load $W = 40$ N and entrainment speed $U\eta = 7.8$ N/m (inlet on left).

N, the radius of the contact zone is approximately 4.5 mm, i.e., about 50% of the ball radius.

Figure 10 shows the maps of lubricant film thickness h for selected values of load W and entrainment speed $U\eta$. It can be seen that a characteristic ridge is formed at the trailing edge of the contact. Depending on the conditions, the minimum film thickness occurs at the rear of the contact or at the side lobes. The latter situation corresponds to higher loads and lower entrainment speeds, in agreement with the results of Hooke [29].

Pressure and film-thickness profiles along the symmetry plane $y = 0$ are shown in Fig. 11. To illustrate the finite deformation effects, results of two simplified models are included in Fig. 11 in addition to the results obtained using the present fully nonlinear model (denoted by solid lines). The first simplified model accounts for finite deformations and the related material and geometrical nonlinearities, however, the friction stresses acting on the ball are neglected (the corresponding results are denoted by dashed lines). In the second simplified model, a geometrically linear theory is adopted so that deformations of the ball are governed by small-strain linear elasticity and configuration changes are neglected. Friction stresses are also neglected, and this model (denoted by dash-dotted lines) is thus equivalent to the classical EHL theory.

It can be seen in Fig. 11 that the effect of friction increases with increasing $U\eta$ but, in general, is not much pronounced. The results obtained without friction stresses are essentially shifted to the left with respect to the

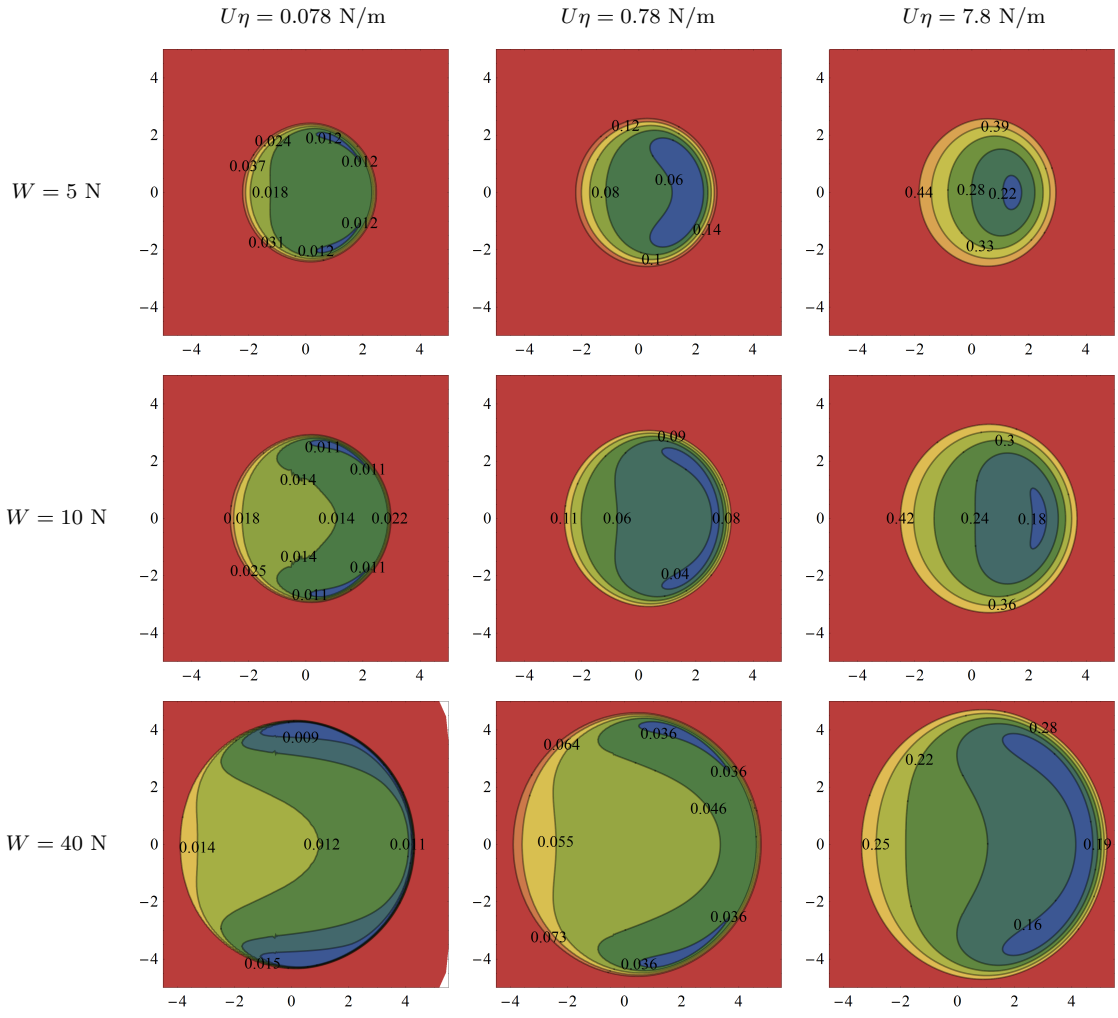

Figure 10: Maps of lubricant film thickness h in mm (inlet on left, position in mm).

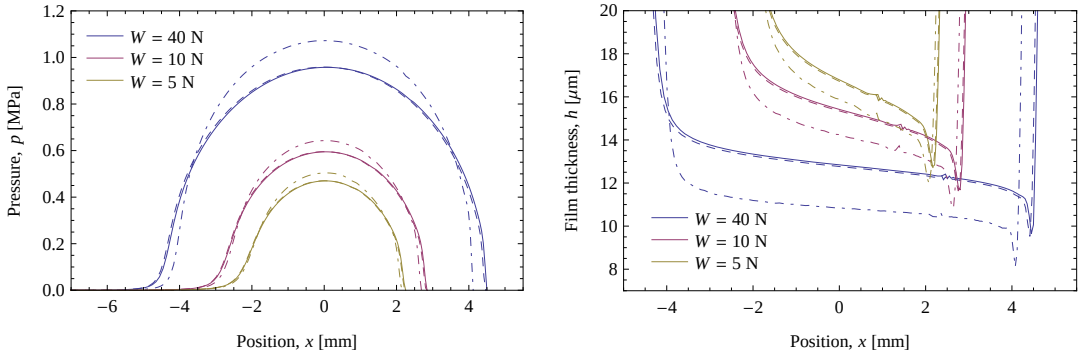

(a)

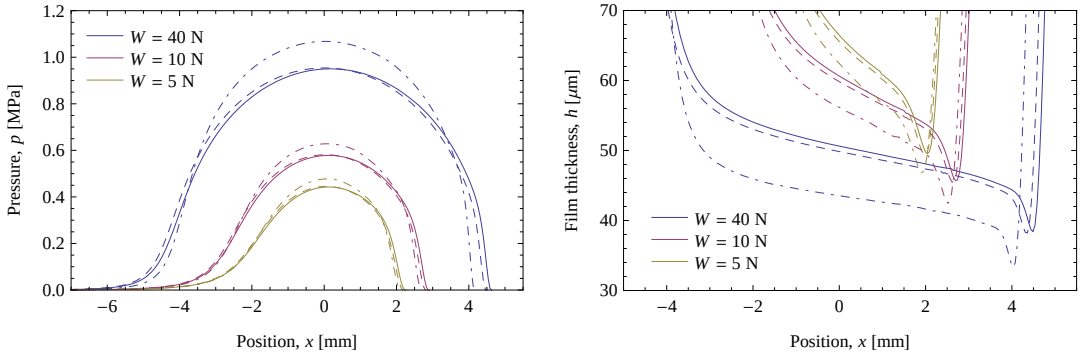

(b)

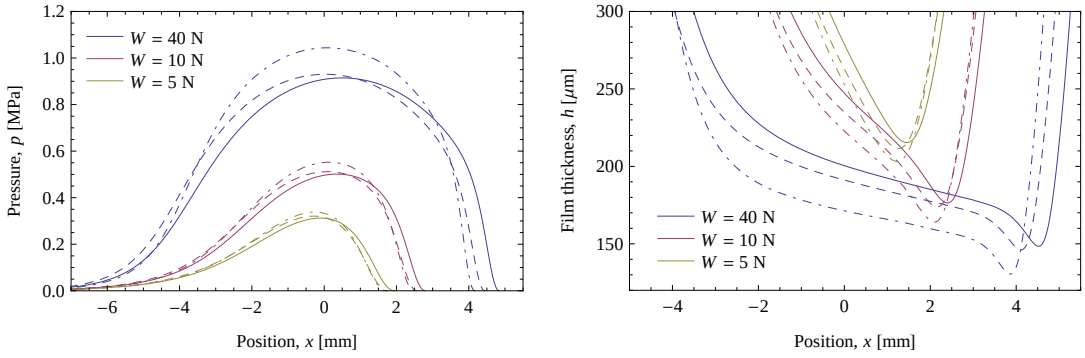

(c)

Figure 11: Profiles of pressure p (left) and film thickness h (right) in the symmetry plane $y = 0$ for (a) $U\eta = 0.078$ N/m, (b) $U\eta = 0.78$ N/m, and (c) $U\eta = 7.8$ N/m. Solid lines denote the fully nonlinear model, dashed lines denote the nonlinear model without friction stresses, dash-dotted lines denote the geometrically linear model.

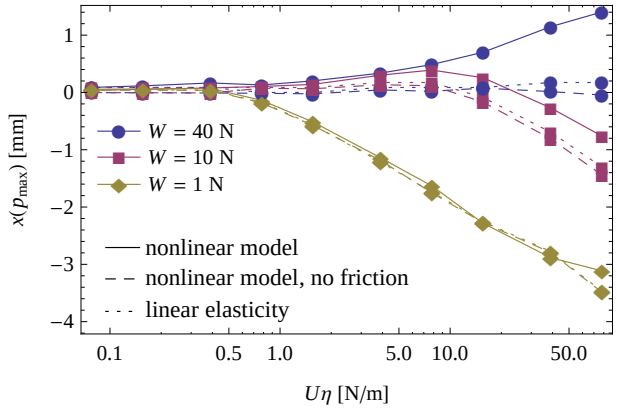

Figure 12: Position of the point of maximum pressure as a function of $U\eta$ and W.

full model, which is related to overall lateral bending-like deformation of the ball caused by friction (note that the ball is rather stiff to bending as the displacements are constrained at its mid-plane). Otherwise, the characteristic values, such as the maximum pressure and the minimum film thickness, are not much affected by friction, although the difference is visible at high entrainment speeds.

On the contrary, the difference between the nonlinear formulation and the geometrically linear one is more pronounced. The difference in the maximum pressure and in the minimum film thickness may exceed 10% and 15%, respectively. Clearly, the discrepancy between the two models increases with increasing load, as the deformations are larger for larger loads.

The difference between the three models is further illustrated in Fig. 12 which shows the location of the point of maximum pressure. At low entrainment speed, the point of maximum pressure is located close to $x = 0$ for all models, which is also visible in Fig. 11. With increasing entrainment speed, the differences between the models become apparent, particularly at higher loads.

Figure 13 shows the friction coefficient as a function of the entrainment speed $U\eta$ and load W. Here, the prediction of the present fully nonlinear model is compared to that of the geometrically linear model. Quite surprisingly, the predicted friction coefficients are practically identical despite the differences in pressure and film thickness, see Fig. 11. Prediction of the regression equation (1) derived in [7] is also included in Fig. 13 and shows a

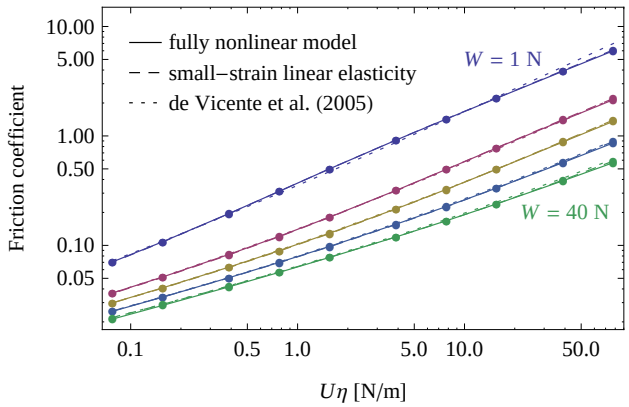

Figure 13: Friction coefficient as a function of $U\eta$ and W: predictions for load W equal to 1, 5, 10, 20 and 40 N.

very good agreement in the whole range of contact conditions.

Considering the excellent agreement of the present results with the regression equation (1), a detailed comparison of the present model with the experiment reported in Section 2 need not be performed. In fact, the comparison presented in Fig. 2 for the regression equation (1) fully characterizes a similar comparison that might be performed for the present model.

5. Conclusion

Effects resulting from finite deformations accompanying lubricated contact in the soft-EHL regime have been studied using a fully-coupled geometrically nonlinear finite-element model. The results obtained for two representative soft-EHL problems indicate that the solution may be significantly influenced by finite deformations of the contacting bodies. To illustrate that, the results of the present fully nonlinear model have been compared to the results obtained for a geometrically linear model which employs linear elasticity and neglects finite configuration changes, and thus corresponds to the classical EHL theory.

The differences between the film thickness and pressure profiles predicted by the two models are clearly visible in the case of an elastic ball sliding against a rigid plane. In a more complex problem of a rigid cylinder sliding against a coated layer, the differences are even more pronounced. In particular, in all cases considered, the film thickness is underestimated by the

geometrically linear model. At higher loads, the difference may reach 20% for the elastic ball example and even 60–70% for the coated layer example. Such differences may be crucially important in the thin-film regime when surface roughness influences lubricant flow.

However, it is noted that, in the case of an elastic ball sliding against a rigid plane, the friction coefficient can be very accurately predicted by the classical EHL theory even at high loads, for instance, using the regression equation derived in [7] for circular point contacts. This is a surprising result in view of the noticeable differences between the two models in terms of film thickness and pressure.

An experimental test rig suitable for examining lubrication under relatively high loads has also been developed, and sample results have been reported for a compliant rubber ball sliding against a steel disc. In the EHL regime, the values of the friction coefficient predicted by the theory show some discrepancy with respect to the experimental ones, particularly at lower loads. At the same time, the dependence on the entrainment speed and on the load shows a good agreement. The observed discrepancy is probably due to complexity of the mechanical behaviour of the examined rubber, which exhibits viscoelastic effects, and these effects cannot be captured by a simple hyperelastic model adopted in the simulation.

Acknowledgement

This work has been partially supported by the National Science Centre (NCN) in Poland under grant No. 2011/01/B/ST8/07434.

Appendix A. Surface gradient and surface divergence

The Reynolds equation has been formulated in Section 3.2 on the surface S which is, in general, a two-dimensional manifold immersed in a three-dimensional Euclidean space. Accordingly, the surface gradient and surface divergence operators appear in the formulation, and the corresponding definitions are provided below, for the details see, e.g., [30].

The surface S is (locally) parametrized by two coordinates ξ^α, $\alpha = 1, 2$, so that $\hat{\boldsymbol{x}} = \hat{\boldsymbol{x}}(\xi^\alpha)$ for $\hat{\boldsymbol{x}} \in S$. The parametrization defines the tangent basis $\boldsymbol{\tau}_\alpha$ and the co-basis $\boldsymbol{\tau}^\alpha$ through

$$\boldsymbol{\tau}_\alpha = \frac{\partial \hat{\boldsymbol{x}}}{\partial \xi^\alpha}, \qquad \boldsymbol{\tau}^\alpha \cdot \boldsymbol{\tau}_\beta = \delta^\alpha_\beta, \tag{A.1}$$

where δ^α_β is the Kronecker delta.

Consider now a scalar field ϕ and a vector field $\boldsymbol{v}$ defined on S. The surface gradient of ϕ is defined by

$$\mathrm{grad}_S \phi = \frac{\partial \phi}{\partial \xi^\alpha} \boldsymbol{\tau}^\alpha, \tag{A.2}$$

and the surface divergence of $\boldsymbol{v}$ is defined by

$$\mathrm{div}_S \boldsymbol{v} = \frac{\partial \boldsymbol{v}}{\partial \xi^\alpha} \cdot \boldsymbol{\tau}^\alpha, \tag{A.3}$$

where the Einstein summation convention applies. It immediately follows that the surface gradient is tangent to S at $\hat{\boldsymbol{x}}$.

References

[1] Z. M. Jin, D. Dowson, Elastohydrodynamic lubrication in biological systems, Proc. Instn. Mech. Engrs. Part J: J. Engng. Tribol. 219 (2005) 367–380.

[2] M. J. Adams, B. J. Briscoe, S. A. Johnson, Friction and lubrication of human skin, Tribol. Lett. 26 (2007) 239–253.

[3] M. B. Jones, G. R. Fulford, C. P. Please, D. L. S. McElwain, M. J. Collins, Elastohydrodynamics of the eyelid wiper, Bull. Math. Biol. 70 (2008) 323–343.

[4] C. Myant, H. A. Spikes, J. R. Stokes, Influence of load and elastic properties on the rolling and sliding friction of lubricated compliant contacts, Tribol. Int. 43 (2010) 55–63.

[5] J. de Vicente, J. R. Stokes, H. A. Spikes, Soft lubrication of model hydrocolloids, Food Hydrocolloids 20 (2006) 483–491.

[6] J. H. H. Bongaerts, K. Fourtouni, J. R. Stokes, Soft tribology: Lubrication in a compliant PDMS–PDMS contact, Tribol. Int. 40 (2007) 1531–1542.

[7] J. de Vicente, J. R. Stokes, H. A. Spikes, The frictional properties of Newtonian fluids in rolling–sliding soft-EHL contact, Tribol. Lett. 20 (2005) 273–286.

[8] M. Scaraggi, G. Carbone, D. Dini, Experimental evidence of micro-EHL lubrication in rough soft contacts, Tribol. Lett. 43 (2011) 169–174.

[9] B. N. J. Persson, M. Scaraggi, On the transition from boundary lubrication to hydrodynamic lubrication in soft contacts, J. Phys.: Condens. Matter 21 (2009) 185002.

[10] M. Scaraggi, B. N. J. Persson, Theory of viscoelastic lubrication, Tribol. Int. 72 (2014) 118–130.

[11] D. Dowson, G. R. Higginson, Elasto-hydrodynamic Lubrication, Pergamon Press, 1977.

[12] B. J. Hamrock, S. R. Schmid, B. O. Jacobsen, Fundamentals of Fluid Film Lubrication, Marcel Dekker, New York, 2 edition, 2004.

[13] S. Stupkiewicz, A. Marciniszyn, Elastohydrodynamic lubrication and finite configuration changes in reciprocating elastomeric seals, Tribol. Int. 42 (2009) 615–627.

[14] J. de Vicente, J. R. Stokes, H. A. Spikes, Rolling and sliding friction in compliant, lubricated contact, Proc. Instn. Mech. Engrs. Part J: J. Engng. Tribol. 220 (2006) 55–63.

[15] L. E. C. Ruskell, A rapidly converging theoretical solution of the elastohydrodynamic problem for rectangular rubber seals, Proc. Instn. Mech. Engrs. Part C: J. Mech. Engng. Sci. 22 (1980) 9–16.

[16] Y. Yang, W. F. Hughes, An elastohydrodynamic analysis of preloaded sliding seals, ASLE Trans. 27 (1983) 197–202.

[17] E. Prati, A. Strozzi, A study of the elastohydrodynamic problem in rectangular elastomeric seals, Trans. ASME J. Tribol. 106 (1984) 505–512.

[18] R. F. Salant, N. Maser, B. Yang, Numerical model of a reciprocating hydraulic rod seal, Trans. ASME J. Tribol. 129 (2007) 91–97.

[19] S. Stupkiewicz, Finite element treatment of soft elastohydrodynamic lubrication problems in the finite deformation regime, Comp. Mech. 44 (2009) 605–619.

[20] J. Lengiewicz, M. Wichrowski, S. Stupkiewicz, Mixed formulation and finite element treatment of the mass-conserving cavitation model, Tribol. Int. 72 (2014) 143–155.

[21] P. Wriggers, Computational Contact Mechanics, Springer, Berlin Heidelberg New York, 2nd edition, 2006.

[22] H. G. Elrod, M. L. Adams, A computer program for cavitation and starvation problems, in: D. Dowson, M. Godet, C. M. Taylor (Eds.), Proc. of the First Leeds–Lyon Symposium on Tribology – Cavitation and Related Phenomena in Lubrication, Mechanical Engineering, New York, 1974, pp. 37–41.

[23] M. Hajjam, D. Bonneau, A transient finite element cavitation algorithm with application to radial lip seals, Tribol. Int. 40 (2007) 1258–1269.

[24] M. Giacopini, M. T. Fowell, D. Dini, A. Strozzi, A mass-conserving complementarity formulation to study lubricant films in the presence of cavitation, Trans. ASME J. Tribol. 132 (2010) 041702–1–12.

[25] T. J. R. Hughes, A. N. Brooks, A multidimensional upwind scheme with no crosswind diffusion, in: T. J. R. Hughes (Ed.), Finite Elements for Convection Dominated Problems, volume 34 of *AMD*, ASME, New York, 1979.

[26] J. Korelc, Automation of primal and sensitivity analysis of transient coupled problems, Comp. Mech. 44 (2009) 631–649.

[27] J. Korelc, P. Wriggers, Improved enhanced strain four-node element with Taylor expansion of the shape functions, Int. J. Num. Meth. Engng. 40 (1997) 407–421.

[28] E. A. de Souza Neto, D. Perić, M. Dutko, D. R. J. Owen, Design of simple low order finite elements for large strain analysis of nearly incompressible solids, Int. J. Sol. Struct. 33 (1996) 3277–3296.

[29] C. J. Hooke, The elastohydrodynamic lubrication of elliptical point contacts operating in the isoviscous region, Proc. Instn. Mech. Engrs. Part J: J. Engng. Tribol. 209 (1995) 225–234.

[30] P. Steinmann, On boundary potential energies in deformational and configurational mechanics, J. Mech. Phys. Solids 56 (2008) 772–800.